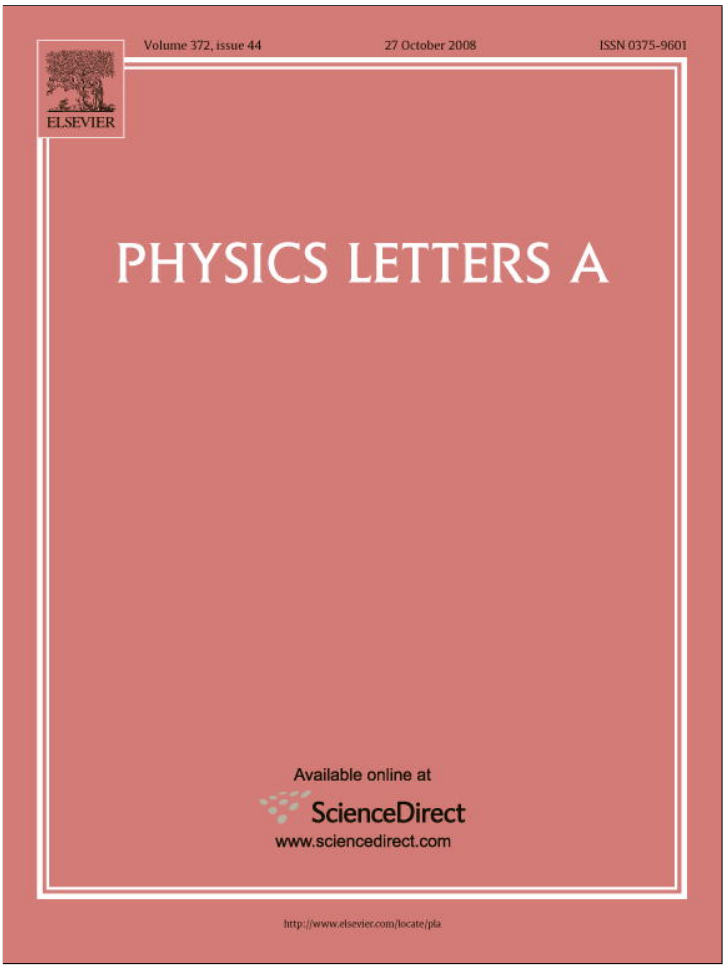

Physics Letters A 372 (2008) 6661–6666

Contents lists available at ScienceDirect

Physics Letters A

www.elsevier.com/locate/pla

Mechanical property of carbon nanotubes with intramolecular junctions: Molecular dynamics simulations

Zhao Qin [a], Qing-Hua Qin [b], Xi-Qiao Feng [a,*]

[a] FML, Department of Engineering Mechanics, Tsinghua University, Beijing 100084, China
[b] Department of Engineering, The Australian National University, Canberra, ACT 0200, Australia

ARTICLE INFO

Article history:
Received 14 May 2008
Received in revised form 1 September 2008
Accepted 3 September 2008
Available online 6 September 2008
Communicated by R. Wu

PACS:
62.25.-g
81.07.De
82.20.Wt

Keywords:
Carbon nanotube
Intramolecular junction
Molecular dynamics simulation
Mechanical property

ABSTRACT

Intramolecular junctions (IMJs) of carbon nanotubes hold a promise of potential applications in nanoelectromechanical systems. However, their structure-property relation is still unclear. Using the revised second-generation Tersoff–Brenner potential, molecular dynamics simulations were performed to study the mechanical properties of single-walled to four-walled carbon nanotubes with IMJs under uniaxial tension. The dependence of deformation and failure behaviors of IMJs on the geometric parameters was examined. It was found that the rupture strength of a junction is close to that of its thinner carbon nanotube segment, and the rupture strain and Young's modulus show a significant dependence on its geometry. The simulations also revealed that the damage and rupture of multi-walled carbon nanotube junctions take place first in the innermost layer and then propagate consecutively to the outer layers. This study is helpful for optimal design and safety evaluation of IMJ-based nanoelectronics.

1. Introduction

Since their discovery in 1991 [1], carbon nanotubes (CNTs) have become a closely watched frontier in many scientific and technological fields due to their striking structure and superior mechanical, physical, and chemical properties [2–9]. They possess extremely high tensile Young's modulus of about 1 TPa or above, and chirality-dependent electrical conductivity [4–14]. Intramolecular junctions (IMJs), which seamlessly fuse two different CNTs together, have also been proposed to display a range of other interesting functions, different from the constituent CNTs [14–25]. For example, two single-walled CNT (SWNT) segments, one metallic and the other semiconducting, can be connected to form an IMJ which behaves like a rectifying diode with nonlinear transport characteristics [15]. Owing to the potential usage of IMJs to miniaturize electronics to the nanometer scale, considerable research efforts have been directed towards the investigation of their formation and properties [16,24]. Iijima et al. [17] observed IMJs repeatedly by transmission electron microscope and ascribed their formation to the decrease and increase of the flux of carbon atoms. Yao et al. [18] experimentally found that varying temperature can tune the diameter and generate IMJs along SWNTs: the diameter of a growing SWNT becomes smaller at higher temperatures, and vice versa. Using scanning tunneling microscopy, Ouyang et al. [19] determined the atomic structures and electronic properties of IMJs, and constructed IMJ models based on the observed structures. Their tight-binding calculations of electronic properties of IMJs showed good agreement with experimental results. Melchor et al. [20] developed a computer algorithm to study the atomic structure of IMJs. Chernozatonskii et al. [21] designed and coated IMJs and other multi-terminal CNTs with thin-walled silica nanotubes to protect these carbon devices from influences of the environment. Via molecular dynamics (MD) simulations, Hanasaki et al. [22] suggested IMJs as molecular nozzles to conduct water flow. They found that the stream velocity increased dramatically in the junction region.

The IMJ configurations of CNTs depend on topological defects at the junctions [19,23]. Although the electronic properties of IMJs have been widely studied, whether and how the defects affect the mechanical properties of the CNTs still remains unclear. In the present Letter, we perform a series of MD simulations to investigate the mechanical properties of single- to multi-walled IMJs with defects and under uniaxial tension. The revised second-generation Tersoff–Brenner (TB-G2) potential [26] is adopted in the simulations.

* Corresponding author.
E-mail address: fengxq@tsinghua.edu.cn (X.-Q. Feng).

0375-9601/$ – see front matter
doi:10.1016/j.physleta.2008.09.010

2. Simulation model

An IMJ of CNTs typically comprises three portions: two segments of CNTs with different diameters, and a conical part connecting the two CNTs [17,19,23]. In this Letter, a single-walled IMJ is characterized by (n_1, m_1)–(n_2, m_2) [19], where (n_1, m_1) and (n_2, m_2) represent the chiral vectors of the thinner and the thicker SWNTs, respectively. Such an IMJ can be synthesized by modifying the temperature during growth, and most IMJs (>95%) are found to be either semiconducting–semiconducting or metallic–metallic type [18]. Figs. 1(a) and (b) show, for example, an armchair (5, 5) SWNT connected to an armchair (9, 9) SWNT and a zigzag (9, 0) SWNT connected to a zigzag (14, 0) SWNT, respectively. The two tubes are connected by introducing a pentagon and a heptagon along the cylindrical axis to the otherwise perfect hexagonal lattice. We use this configuration because it has been found to be the most stable case after full relaxation among different distributions of defects that allow the connection of two CNTs [25].

From a simple geometrical analysis, the IMJ length along the axial direction can be given approximately as

$$l = l_1 + l_2 + l_3, \quad l_3 = \frac{\pi (d_1 - d_2)}{2\tan(\pi/6)}, \tag{1}$$

where l_1 and l_2 are the lengths of the thinner and the thicker SWNTs, respectively [Fig. 1(c)]. d_i $(i = 1, 2)$ is the diameter of a SWNT which is related to the chiral vector (n_i, m_i) by

$$d_i = \sqrt{3\left(n_i^2 + m_i^2 + n_i m_i\right)}\, a_{cc}/\pi, \tag{2}$$

where $a_{cc} = 1.42$ Å is the length of a C–C bond at equilibrium. The geometric parameters of the ten single-walled IMJs studied in this Letter are summarized in Table 1.

For the sake of simplicity, we use the engineering strain $\varepsilon = (l' - l)/l$ to describe the deformation of an IMJ in the axial direction, where l and l' are the initial and the current lengths, respectively. The tensile stress of the IMJ is defined as the applied force F divided by the cross-sectional area of the thinner CNT. The wall thickness of the CNTs is assumed to equal the interlayer distance in graphite, $h = 3.4$ Å [10]. The applied force F is calculated by summing the interatomic forces on all the atoms at the end of the tube where the displacement is imposed. Provided that the strain rate is sufficiently slow, the simulation results have no evident dependence on the strain rate and the equilibration time.

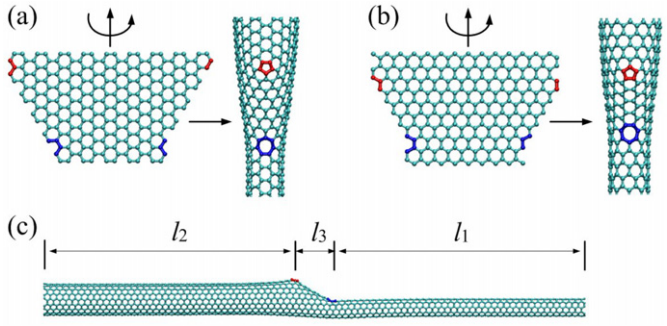

Fig. 1. Simulation model of (a) (5, 5)–(9, 9) IMJ, (b) (9, 0)–(14, 0) IMJ viewed from the front, and (c) (5, 5)–(10, 10) IMJ viewed from the side.

3. MD method

The MD program IMD [27,28] is used to simulate the deformation process of IMJs under uniaxial tension. The forces acting on the carbon atoms are calculated using two different methods, depending upon the distance between atoms. The TB-G2 potential [26] is utilized to describe the covalent bonds within an IMJ over a short range, whereas the Lennard–Jones (LJ) potential is employed for a longer range beyond the cut-off of the TB-G2 potential.

The bond-order TB-G2 potential, which has been successfully used to study the deformation and failure behavior of CNTs [29], takes the form [26]

$$E_b = \sum_i \sum_{j(>i)} f^c(r_{ij})\left[V^R(r_{ij}) - b_{ij} V^A(r_{ij})\right], \tag{4}$$

where V^R and V^A are the pair-additive interactions representing all the interatomic repulsion and attraction, respectively, r_{ij} is the distance between the atoms i and j, and b_{ij} is a bond-order function which depends on the bond lengths and bond angles involving the atoms i and j. The cut-off function $f_c(r_{ij})$ which restricts the pair potential to the nearest neighbors is given by

$$f^c(r_{ij}) = \begin{cases} 1, & r_{ij} < r_1, \\ \frac{1}{2}\left[1 + \cos\frac{(r_{ij} - r_1)\pi}{(r_2 - r_1)}\right], & r_1 < r_{ij} < r_2, \\ 0, & r_{ij} > r_2, \end{cases} \tag{5}$$

where r_1 and r_2 are the onset and the offset of the cut-off function, respectively. As suggested by Sammalkorpi et al. [7], we increase r_1 from 1.8 Å to 2.05 Å to avoid overestimation of the force needed to break a bond [5,29]. Previous studies have demonstrated the efficiency of this treatment to study the mechanical properties of CNTs and other CNT structures [7,30].

The following Lennard–Jones (LJ) potential suggested by Mao et al. [31] is employed in our analysis

$$E_{LJ}(r_{ij}) = \begin{cases} 0, & r_{ij} < r_2, \\ c_{3,k}(r_{ij} - r_k)^3 + c_{2,k}(r_{ij} - r_k)^2, & r_2 < r_{ij} < r_3, \\ \varepsilon_{ij}\left[\left(\frac{\sigma_{ij}}{r_{ij}}\right)^{12} - 2\left(\frac{\sigma_{ij}}{r_{ij}}\right)^6\right], & r_3 < r_{ij} < r_4, \end{cases} \tag{6}$$

Table 1
Geometric and physical parameters of ten IMJs with representative structural parameters. l_1, l_2 and l_3 are the lengths of the thinner CNT, the thicker CNT, and the conical segment, respectively (Fig. 1(c)), d_1 and d_2 the diameters of the two CNT segments with $d_2 \geqslant d_1$, E is the average potential energy of the atoms between the pentagon-heptagon pair in the axial direction after sufficient relaxation

Structure	l_1 (Å)	l_2 (Å)	l_3 (Å)	d_1 (Å)	d_2 (Å)	E (eV/atom)
(5, 5)	46.9	–	–	6.78	–	−7.300
(5, 5)–(6, 6)	100.2	100.1	3.6	6.78	8.14	−7.277
(5, 5)–(7, 7)	100.2	100.0	7.3	6.78	9.49	−7.296
(5, 5)–(8, 8)	100.3	99.9	11.1	6.78	10.85	−7.306
(5, 5)–(9, 9)	100.3	99.8	14.8	6.78	12.20	−7.314
(5, 5)–(10, 10)	100.3	99.7	18.6	6.78	13.56	−7.321
(9, 0)	49.5	–	–	7.05	–	−7.300
(9, 0)–(10, 0)	98.7	98.7	2.2	7.05	7.83	−7.287
(9, 0)–(11, 0)	98.8	98.7	4.3	7.05	8.61	−7.290
(9, 0)–(12, 0)	98.9	98.7	6.4	7.05	9.39	−7.298
(9, 0)–(13, 0)	98.8	98.7	8.5	7.05	10.18	−7.303
(9, 0)–(14, 0)	98.8	98.7	10.7	7.05	10.96	−7.308

where $c_{n,k}$ are cubic spline coefficients. The parameters in Eq. (6) are given as $r_3 = 3.2$ Å, $\varepsilon_{ij} = 4.2038 \times 10^{-3}$ eV, $\sigma_{ij} = 3.783$ Å, and $r_4 = 10.0$ Å. It should be noted that the LJ potential has a nonzero value only after the TB-G2 potential goes to zero.

We simulate a segment of IMJ of single-walled or multi-walled CNTs (MWNTs) under uniaxial tension. The diameters d_1 and d_2 as well as the wall number of the CNT are varied in order to examine the dependence of its mechanical properties on geometric parameters. An example of the simulation sample of a single-walled IMJ is shown in Fig. 1(c). The calculated atomic sample is initially relaxed to optimize its potential energy, using the microconvergence method [27,28]. The carbon atoms at the left end of the system are fixed in the axial direction, while a gradually increasing displacement with a low rate of 16.7 m/s along the axial direction is applied to the atoms at the right end. All the atoms are free in the radial and circumferential directions. Using a Nose–Hoover extended ensemble [32], simulations are performed at a constant temperature of 300 K. The force–displacement curve is recorded during the entire tension process, and thereby the elastic modulus, rupture strength and strain can be determined.

4. Results and discussion

4.1. Single-walled IMJs

We begin with comparisons of the mechanical properties of single-walled IMJs with several representative combinations of the diameters d_1 and d_2, with $d_2 \geqslant d_1$. Their geometric parameters are listed in Table 1. Two typical groups of IMJs, each consisting of either two armchair or two zigzag CNTs, are chosen, which are marked as armchair–armchair (A–A) and zigzag–zigzag (Z–Z) IMJs and have different electric properties. In each group, we hold the value of d_1 fixed and vary d_2 consecutively. It is noted that after full initial relaxation, the average equilibrium energy E of the atoms around the junction depends on the combination of the diameters d_1 and d_2. For a fixed d_1, the average equilibrium energy E decreases with the increase of d_2. This can be easily understood from the fact that the average energy E of a normal and defect-free CNT decreases quadratically with respect to its radius [33].

In spite of the predominant advantages of the TB-G2 potential, the artificial introduction of the cut-off function in it leads to a remarkable increase in the interatomic force at $r = r_1$ and a somewhat overestimation on the maximal tensile strength, as has been argued, following simulations of SWNTs and other CNT structures, in [5,7,29,30]. For this reason, we compare the results calculated by taking $r_1 = 1.8$ Å and $r_1 = 2.05$ Å in order to examine the effect of the cut-off function. The curves obtained for the stretching force F with respect to the tensile strain ε for the $(5,5)$–$(10,10)$ IMJ are given in Fig. 2. The two force–strain curves, each with the different cut-off onsets, have good coincidence until the strain reaches a threshold value (e.g., point A in Fig. 2). Thereafter, the two curves deviate gradually from each other. One may ascribe the flat region following the threshold to the bond elongation corresponding to the cut-off value. The beginning of the plateau is interpreted as the bond rupture point, with the corresponding rupture force denoted as F_{rup}, the rupture strain as ε_{rup}, the rupture potential energy as E_{rup}, and the rupture stress as σ_{rup}. For clarity, the F–ε curves with $r_1 = 2.05$ Å for all the A–A and Z–Z IMJs are given in Figs. 3(a) and 3(b), respectively. The mechanical parameters for these IMJs are summarized in Table 2.

The force–strain curve of an IMJ before the occurrence of rupture can be divided into three regions. The first stage corresponds to elastic deformation, which is mainly attributed to the relative rotation and small elongation of the C–C bonds. In this stage, the applied force F increases linearly with increasing tensile strain, as shown in Figs. 2 and 3. The Young's modulus Y at this stage is calculated by linear fitting of the F–ε curve with $\varepsilon < 10\%$, as shown in the square inserts of Figs. 3(a) and (b) for the selected A–A and Z–Z IMJs. In Eq. (7) below, Y is defined as the slope of the line divided by the cross-sectional area of the thinner CNT. For a specified diameter d_1 of the thinner CNT, Y increases with the increase in the diameter d_2 of the thicker CNT, as shown in Table 2 for each group of A–A and Z–Z IMJs. This variation tendency of Y can be explained by continuum elasticity theory. By using the series model of springs and noticing that the lengths l_1 and l_2 are much greater than l_3, the Young's modulus of an IMJ can be estimated by

$$Y = \frac{ld_2}{l_1 d_2 + l_2 d_1} Y_C, \tag{7}$$

where Y_C is the Young's modulus for a normal, defect-free SWNT [33]. The Young's modulus Y_C can be obtained from continuum theory [14] or direct atomistic simulation. According to our MD simulations, the Young's moduli of the defect-free $(5,5)$ and $(9,0)$ SWNTs are $Y_C = 638.0$ GPa and $Y_C = 668.5$ GPa, which can be adopted in Eq. (7) for the two considered groups of A–A and Z–Z IMJs, respectively. Thus from Eq. (7), one can easily understand the

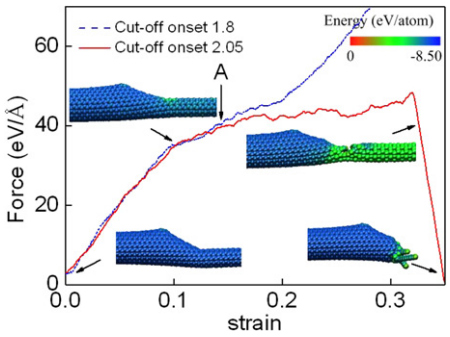

Fig. 2. Force–strain curves of the $(5,5)$–$(10,10)$ IMJ under uniaxial tension with cut-off onsets of $r_1 = 1.8$ Å and $r_1 = 2.05$ Å. Insets are snapshots of the deformation process. The atoms are colored according to their potential energy. (For interpretation of the references to color in this figure, the reader is referred to the web version of this Letter.)

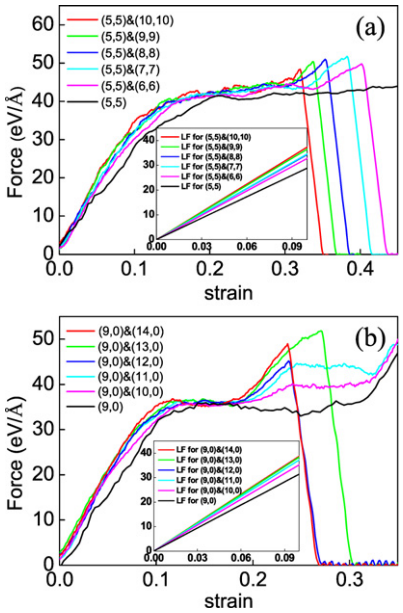

Fig. 3. Force–strain curves of (a) armchair IMJs of $(5,5)$–$(6,6)$, $(5,5)$–$(7,7)$, $(5,5)$–$(8,8)$, $(5,5)$–$(9,9)$ and $(5,5)$–$(10,10)$, and SWNT of $(5,5)$ under uniaxial tension and (b) zigzag IMJs of $(9,0)$–$(10,0)$, $(9,0)$–$(11,0)$, $(9,0)$–$(12,0)$, $(9,0)$–$(13,0)$ and $(9,0)$–$(14,0)$, and SWNT of $(9,0)$ under uniaxial tension. The inset shows the linear fit (LF) of the force–strain curves before 10% strain.

Table 2
Mechanical parameters of ten IMJs with representative structural parameters. E_{rup} represents the potential energy at rupture, F_{rup} the rupture force σ_{rup}, the rupture stress, ε_{rup} the rupture strain, and Y the Young's modulus before strain 10%

Structure	E_{rup} (eV/atom)	F_{rup} (eV/Å)	σ_{rup} (GPa)	ε_{rup} (%)	Y (GPa)
(5, 5)	−6.429	41.2	91.1	22.1	638.0
(5, 5)–(6, 6)	−6.687	40.6	89.8	17.2	724.6
(5, 5)–(7, 7)	−6.775	40.7	90.0	16.1	764.1
(5, 5)–(8, 8)	−6.834	40.8	90.3	15.4	759.3
(5, 5)–(9, 9)	−6.881	40.6	89.8	14.8	807.7
(5, 5)–(10, 10)	−6.925	39.7	87.8	14.3	825.5
(9, 0)	−6.854	35.2	74.9	13.9	668.5
(9, 0)–(10, 0)	−6.853	35.7	76.0	13.4	750.0
(9, 0)–(11, 0)	−6.888	36.2	77.1	12.7	792.2
(9, 0)–(12, 0)	−6.913	35.6	75.8	12.5	791.5
(9, 0)–(13, 0)	−6.971	36.0	76.6	11.3	816.5
(9, 0)–(14, 0)	−7.014	35.8	76.2	10.5	825.1
[(5, 5)–(10, 10)]@[(10, 10)–(15, 15)]	−6.869	125.1	92.4	16.7	805.7
[(5, 5)–(10, 10)]@[(10, 10)–(15, 15)]@[(15, 15)–(20, 20)]	−6.902	248.8	91.9	16.2	765.0
[(5, 5)–(10, 10)]@[(10, 10)–(15, 15)]@[(15, 15)–(20, 20)]@[(20, 20)–(25, 25)]	−6.839	421.5	93.4	17.7	748.2

simulation results that the Young's modulus Y of IMJs increases as the diameter ratio d_1/d_2 decreases.

In the second stage, the F–ε relation becomes nonlinear due to the nonlinear constitutive relation of SWNTs at higher tension strains. As can be seen from Table 2, the IMJs in each of the two groups of A–A type and Z–Z type have almost identical values of F_{rup} and σ_{rup}. This indicates that the strength of an IMJ depends mainly on the strength of its weakest segment, i.e., the thinner CNT. However, both ε_{rup} and E_{rup} of the two groups of IMJs decrease with the decrease in d_1/d_2. For example, the (5, 5)–(6, 6) IMJ has $\varepsilon_{rup} = 17.2\%$ and $E_{rup} = -6.687$ eV/atom, whereas the (5, 5)–(10, 10) IMJ has $\varepsilon_{rup} = 14.3\%$ and $E_{rup} = -6.925$ eV/atom. The underlying reason for this phenomenon lies in the fact that for a smaller value of d_1/d_2, the applied tensile deformation becomes more centralized in the thinner segment, and simultaneously the thicker segment undergoes less deformation. Therefore, the rupture energy and rupture strain depend mainly on the thinner and weaker CNT. Our simulations also show that the rupture of a single-walled IMJ always initiates at the junction end connected to the thinner CNT, as shown by the insert of snapshots in Fig. 2. This phenomenon is also understandable by considering the asymmetrical geometry of the junction and the stress concentration at that position. In the IMJ configurations considered, the thicker segment is not ideally coaxial with the thinner one, leading to a bending moment and hence a nonuniform tensile stress distribution on the cross section of the CNT. Therefore, the C–C bonds of the upper part of the thinner segment are more susceptible to breakage, especially at the connecting end where a heptagonal defect exists. Then the rupture propagates until the complete breakage of the junction occurs (see the snapshots in Fig. 2), which is very similar to the tension-bending rupture mode of defect-free SWNTs [13].

The plateau following the initiation of rupture results from the artificial elongation of some C–C bonds [30], and the rapid drop of the applied force in the force–strain curve corresponds to the unstable breaking of C–C bonds. However, as mentioned previously, the F–ε curve in this region is very sensitive to the onset value r_1 of the cut-off function in the potential (5) [7,29]. Therefore, the rupture curves in this region may not be accurate and should be viewed as a rough estimation only.

4.2. Multi-walled IMJs

We further study the mechanical properties of multi-walled IMJs under uniaxial tension. To examine the effect of the wall number N, the following four IMJs are simulated and compared:

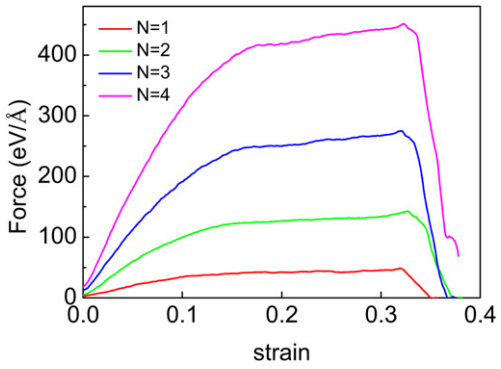

Fig. 4. Force–strain curves of multi-walled IMJs with the number of layers N varying from 1 to 4.

(i) a single-walled IMJ, (5, 5)–(10, 10);
(ii) a double-walled IMJ, [(5, 5)–(10, 10)]@[(10, 10)–(15, 15)];
(iii) a triple-walled IMJ, [(5, 5)–(10, 10)]@[(10, 10)–(15, 15)]@[(15, 15)–(20, 20)], and
(iv) a four-walled IMJ, [(5, 5)–(10, 10)]@[(10, 10)–(15, 15)]@[(15, 15)–(20, 20)]@[(20, 20)–(25, 25)].

The force–strain relations of the four IMJs are shown in Fig. 4, where the cut-off onset $r_1 = 2.05$ Å, and their mechanical properties are summarized in Table 2. It is observed from Table 2 that as the number of layers N increases from 1 to 4, the rupture strain σ_{rup} and Young's modulus Y vary in different manners. For example, the values of σ_{rup} and Y of the four-walled IMJ are 3.4% higher and 77.3 GPa lower than those of the single-walled IMJ, respectively. The rupture force F_{rup} increases from 39.7 eV/Å for the single-walled IMJ to 421.5 eV/Å for the four-walled IMJ. However, there is little difference among the values of σ_{rup} and E_{rup} for these IMJs.

Finally, the rupture features of multi-walled IMJs are explored. Figs. 5(a)–(d) show, for example, the failure process of the four-walled IMJ with the increase in the applied displacement. It should be noted that the applied strains in these figures have already exceeded the rupture strain. It is obvious that as the strain increases, the innermost layer of the tube breaks first before the onset of damage in the other layers. After the innermost layer fails totally, the next inner layer starts to break, and this process continues until the outermost layer breaks. This is a different phenomenon from that which occurs in perfect MWNTs, in which the rupture occurs first in the outermost layer [6]. The above rupture feature of IMJs is understandable by considering the fact that the different

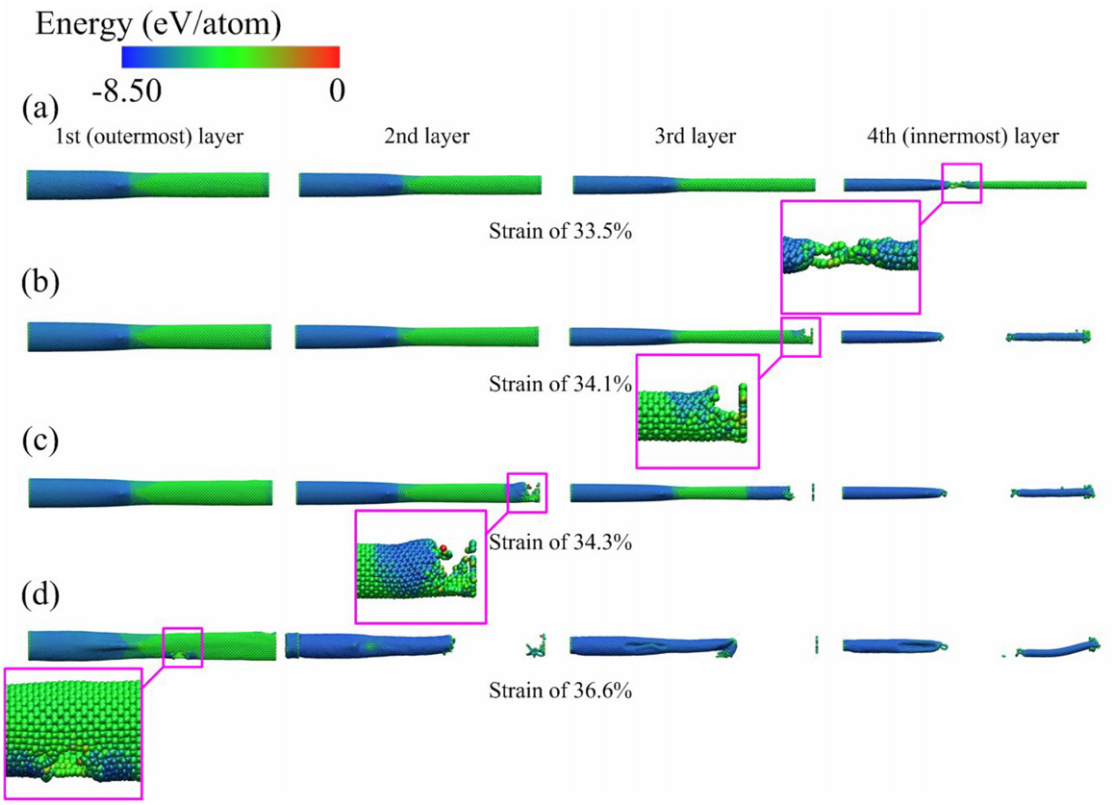

Fig. 5. Simulation snapshots of the four-walled IMJ of [(5, 5)–(10, 10)]@[(10, 10)–(15, 15)]@[(15, 15)–(20, 20)]@[(20, 20)–(25, 25)] under tension at 300 K. The atoms are colored according to their potential energy. (For interpretation of the references to color in this figure, the reader is referred to the web version of this Letter.)

layers of an IMJ have different diameter ratios d_1/d_2 and different magnitudes of stress concentration. For the four-walled IMJ, the outermost layer has $d_1/d_2 = 0.8$ while the innermost layer has only $d_1/d_2 = 0.5$. Thus the tensile strain and stress are more uniform in the outermost layer but more centralized in the thinner segment of the innermost layer. Therefore, it is the differential stress concentrations that determine the rupture sequence from inside to outside. In contrast, however, there is no differential stress concentration in each layer of a perfect MWNT.

5. Conclusions

The mechanical properties of the IMJs of CNTs under uniaxial tension are investigated using MD simulations based on the TB-G2 potential. It is found that the rupture strength of a single-walled IMJ is similar to that of its thinner segment, while the rupture strain decreases and Young's modulus increases with the decrease in the diameter ratio d_1/d_2 of the two constituent CNT segments. The rupture of a single-walled IMJ generally initiates at the junction end connected to the thinner CNT. Different mechanical properties (e.g., rupture strain, rupture stress, rupture energy, and Young's modulus) of IMJs show different dependences on the number of layers. It is also shown that the rupture of a multi-walled junction takes place first in the innermost layer and then propagates outwards with increasing applied strain. This study is helpful not only for understanding the mechanical properties of IMJs but also for optimal design of IMJ-based nanodevices and systems with enhanced performance.

Acknowledgements

Financial support for this work was provided by the National Natural Science Foundation of China (Grant Nos. 10525210 and 10732050). X.-Q. Feng gratefully acknowledges the support of Executive Endeavour Awards of Australia for his visit to the Australian National University.

References

[1] S. Iijima, Nature 354 (1991) 56.
[2] P.M. Ajayan, Chem. Rev. 99 (1999) 1787.
[3] J. Zou, B.H. Ji, X.Q. Feng, H. Gao, Nano Lett. 6 (2006) 430.
[4] M.F. Yu, O. Lourie, M.J. Dyer, K. Moloni, T.F. Kelly, R.S. Ruoff, Science 287 (2000) 637.
[5] T. Belytschko, S.P. Xiao, G.C. Schatz, R.S. Ruoff, Phys. Rev. B 65 (2002) 235430.
[6] K.M. Liew, X.Q. He, C.H. Wong, Acta Mater. 52 (2004) 2521.
[7] M. Sammalkorpi, A. Krasheninnikov, A. Kuronen, K. Nordlund, K. Kaski, Phys. Rev. B 70 (2004) 245416.
[8] D.L. Shi, X.Q. Feng, Y. Huang, K.C. Hwang, H. Gao, J. Eng. Mater. Technol. 126 (2004) 250.
[9] D.L. Shi, X.Q. Feng, H.Q. Jiang, Y.Y. Huang, K.C. Hwang, Int. J. Fracture 134 (2005) 369.
[10] J.P. Lu, Phys. Rev. Lett. 79 (1997) 1297.
[11] H. Jiang, K.C. Hwang, Y. Huang, Key Eng. Mater. 340 (2007) 11.
[12] M.J. Buehler, J. Mater. Res. 21 (2006) 2855.
[13] H. Jiang, X.Q. Feng, Y. Huang, K.C. Hwang, P.D. Wu, Comput. Methods Appl. Mech. Engrg. 193 (2004) 3419.
[14] J. Wu, K.C. Hwang, Y. Huang, J. Mech. Phys. Solids 56 (2008) 279.
[15] Z. Yao, H.W.C. Postma, L. Balents, C. Dekker, Nature 402 (1999) 273.
[16] P.G. Collins, A. Zettl, H. Bando, A. Thess, R.E. Smalley, Science 278 (1997) 100.
[17] S. Iijima, T. Ichihashi, Nature 356 (1992) 776.
[18] Y.G. Yao, Q.W. Li, J. Zhang, R. Liu, L.Y. Jiao, Y.T. Zhu, Z.F. Liu, Nature Mater. 6 (2007) 283.
[19] M. Ouyang, J.L. Huang, C.L. Cheung, C.M. Lieber, Science 291 (2001) 97.
[20] S. Melchor, J.A. Dobado, J. Chem. Inf. Comput. Sci. 44 (2004) 1639.
[21] L.A. Chernozatonskii, V.I. Artyukhov, P.B. Sorokin, Phys. Rev. B 74 (2006) 045402.
[22] I. Hanasaki, A. Nakatani, Nanotechnology 17 (2006) 2794.
[23] H. Kim, J. Lee, Y.J. Song, B.Y. Choi, S.J. Kahng, Y. Kuk, Thin Solid Films 464 (2004) 335.
[24] G.Y. Tseng, J.C. Ellenbogen, Science 294 (2001) 1293.
[25] C. Garau, A. Frontera, D. Quinonero, A. Costa, P. Ballester, P.M. Deya, Chem. Phys. 303 (2004) 265.

[26] D.W. Brenner, O.A. Shenderova, J.A. Harrison, S.J. Stuart, B. Ni, S.B. Sinnott, J. Phys.: Condens. Matter 14 (2002) 783.
[27] J. Roth, F. Gahler, H.R. Trebin, Int. J. Mod. Phys. C 11 (2000) 317.
[28] J. Stadler, R. Mikulla, H.R. Trebin, Int. J. Mod. Phys. C 8 (1997) 1131.
[29] S.L. Zhang, S.L. Mielke, R. Khare, D. Troya, R.S. Ruoff, G.C. Schatz, T. Belytschko, Phys. Rev. B 71 (2005) 115403.
[30] Z. Qin, X.Q. Feng, J. Zou, Y. Yin, S.W. Yu, Appl. Phys. Lett. 91 (2007) 043108.
[31] Z.G. Mao, A. Garg, S.B. Sinnott, Nanotechnology 10 (1999) 273.
[32] S. Nose, Mol. Phys. 100 (2002) 191.
[33] J.M. Molina, S.S. Savinsky, N.V. Khokhriakov, J. Chem. Phys. 104 (1996) 4652.